Cancer Biol Med 2025. doi: 10.20892/j.issn.2095-3941.2025.0026

ORIGINAL ARTICLE

Beyond gold: the chemoenhancing mechanism and therapeutic potential of auranofin in melanoma

Xiaofeng Wang[1,2*], Yingnan Liu[1,2*], Wuqiong Zhang[1,2], Zhongda Li[1,2], Su Li[1,2], Jiaxin Chen[1,2], Qi Li[1,2], Xiaoman Suo[1,2], Yanqiao Zeng[1,2], Guofang Zhang[1,2], Yang Li[1,2,3]

[1]Laboratory of Inflammation and Vaccines, Shenzhen Institutes of Advanced Technology, Chinese Academy of Sciences, Shenzhen 518005, China; [2]Laboratory of Immunology and Nanomedicine and China-Italy Joint Laboratory of Pharmacobiotechnology for Medical Immunomodulation, Shenzhen Institutes of Advanced Technology, Chinese Academy of Sciences, Shenzhen 518005, China; [3]Key Laboratory of Biomedical Imaging Science and System, Chinese Academy of Sciences and State Key Laboratory of Biomedical Imaging Science and System, Shenzhen 518005, China

ABSTRACT

Objective: The objective of the current study was to evaluate the chemosensitizing capacity of auranofin (AF), a gold (I) complex traditionally used in rheumatoid arthritis treatment, in potentiating the cytotoxic effects of doxorubicin (DOX) in melanoma cell models, specifically drug-sensitive (B16F10) and multidrug-resistant (B16F10/ADR) variants.

Methods: Experimental measurements, including *in vitro* cytotoxicity and apoptosis assays, surface plasmon resonance (SPR), immunoblotting assays, as well as theoretical calculations, such as molecular docking and molecular dynamics (MD) simulations, were used to systematically delineate the interaction dynamics between AF and thioredoxin reductase 1 (TrxR1). The anti-tumor efficacy of co-treatment with AF and DOX was assessed by examining cell viability and apoptotic rates.

Results: Co-treatment with AF and DOX significantly increased anti-tumor efficacy, as evidenced by reduced cell viability and increased apoptotic rates. This synergistic effect was attributed to inhibition of TrxR1 by AF, which compromised tumor cell antioxidant defenses and elevated intracellular reactive oxygen species (ROS), thereby enhancing apoptotic pathways. Notably, AF treatment mitigated the heightened TrxR activity in DOX-resistant cells, intensifying the pro-oxidant effects of DOX, leading to increased ROS production and cell death. The data also showed that AF binds with high affinity to the selenocysteine residue within the catalytic site of TrxR1, which partially overlapped with the binding site of the endogenous substrate, thioredoxin (Trx), but with greater avidity. This unique binding configuration impedes the reduction of Trx by TrxR1, triggering an apoptotic response in cancer cells.

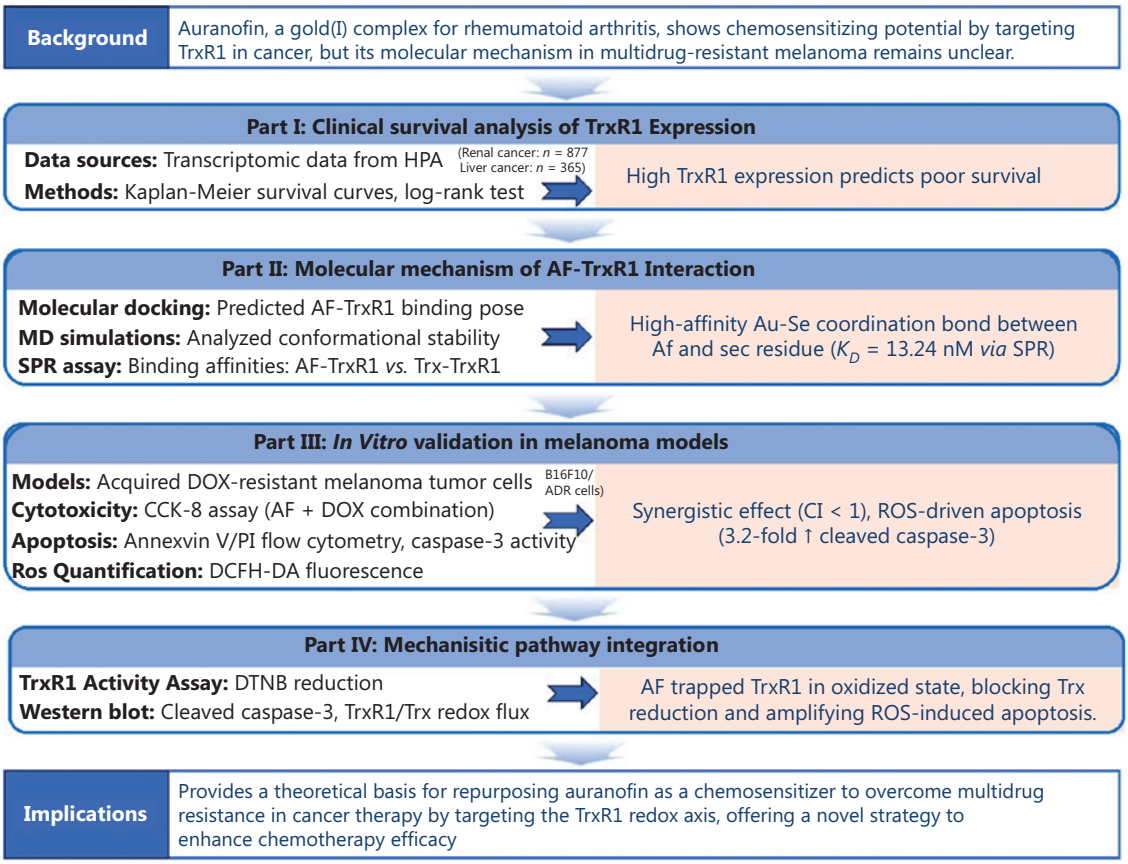
Conclusions: This study underscores the chemosensitizing potential of AF in overcoming multidrug resistance in cancer therapy through redox modulation. The molecular mechanism of action underlying AF on TrxR1 demonstrated the unique binding configuration that impedes the reduction of Trx by TrxR1 and instigates an apoptotic response in cancer cells. These findings pave the way for the clinical application of AF as a chemosensitizer, offering a novel approach to augment the efficacy of existing chemotherapy regimens.

KEYWORDS Auranofin; TrxR1; anti-cancer; drug resistance; molecular dynamics simulation

Introduction

Chrysotherapy has attracted scientists and led to a research focus on gold-containing medications[1-7], typically including gold glucose (aurothioglucose)[8], gold sodium thiomalate (aurothiomalate)[2,9], sodium bis-thiosulfate gold (aurothiosulfate)[10,11], and auranofin (AF)[3,12-15]. These medications contribute to various disease treatments involving asthma[4], malaria[5], arthritis, cancer[6], and AIDS[7]. AF [molecular formula $C_{20}H_{34}AuO_9$, An Au(I) complex] is the first gold-containing drug for rheumatoid arthritis (RA) treatment[16]. AF inhibits the activity of hydrolytic enzymes, such as β-glucuronidase and elastase[17]. AF was approved by U.S. Food & Drug Administration (FDA) for the treatment of RA in 1985 with the brand name, Ridaura[18]. It was shown that RA patients treated with AF have lower malignancy rates than non-treated patients[19], which paved the way for use of AF as an anticancer

*These authors contributed equally to this work.
Correspondence to: Yang Li
E-mail: yang.li@siat.ac.cn
ORCID ID: https://orcid.org/0000-0001-7242-4687
Received February 13, 2025; accepted April 21, 2025;
published online June 27, 2025.
Available at www.cancerbiomed.org
©2025 The Authors. Creative Commons Attribution-NonCommercial 4.0 International License



Study Flow Part I conducts a clinical survival analysis of TrxR1 expression, assessing its correlation with survival in renal, liver, and melanoma cancers using transcriptomic data from HPA *via* Kaplan-Meier survival curves and the log-rank test, finding that high TrxR1 expression predicts poor survival. Part II focuses on the molecular mechanism of AF-TrxR1 interaction, characterizing AF's binding to TrxR1 at the selenocysteine active site through molecular docking and MD simulations, revealing a high-affinity Au-Se coordination bond between AF and Sec residue and verified *via* SPR. Part III performs *in vitro* validation in melanoma models, including drug-sensitive and acquired DOX-resistant melanoma tumor cells (B16F10/ADR cells), using cytotoxicity (MTT assay), apoptosis, and ROS quantification methods, showing a synergistic effect (CI < 1) and ROS-driven apoptosis. Part IV integrates the mechanistic pathway, elucidating redox dysregulation and apoptotic activation by TrxR1 activity assay and western blot, demonstrating that AF trapped TrxR1 in the oxidized state, blocking Trx reduction and amplifying ROS-induced apoptosis. The study provides a theoretical basis for repurposing auranofin as a chemosensitizer to overcome multidrug resistance in cancer therapy by targeting the TrxR1 redox axis, offering a novel strategy to enhance chemotherapy efficacy. TrxR1, thioredoxin reductase 1; AF, auranofin; DOX, doxorubicin; ROS, reactive oxygen species; MD, molecular dynamics; SPR, surface plasmon resonance; CI, combination index (Chou-Talalay).

application. Indeed, AF is expected to become a promising anticancer drug[20-29].

In recent years the issue of drug resistance in cancer has become increasingly prominent[30-34]. How to reverse tumor drug resistance has become a primary concern in the development of anticancer drugs[35-38]. Recently, Deepika et al.[39] reported that AF sensitizes breast cancer cells to paclitaxel by upregulating FOXO3, thereby inhibiting Nrf2 translocation and promoting apoptosis. This finding revealed the potential of AF as a chemosensitizer through modulation of the FOXO3/Nrf2/Keap1 signaling pathway with implications for clinical application following preclinical evaluation[39]. High-grade serous ovarian cancer (HGSOC), the most common and lethal form of ovarian cancer, often develops resistance to platinum-based chemotherapy. Abdalbari et al.[23] investigated the potential of AF in targeting multiple cytotoxic pathways in HGSOC cells (platinum-sensitive and -resistant) by inhibiting thioredoxin reductase (TrxR) and depleting antioxidants, thus suggesting a novel therapeutic strategy for long-term consolidation therapy against HGSOC. The proposed mechanisms

underlying the anti-cancer activity by AF involve an increase in intracellular thiols, such as glutathione and thioredoxin (Trx)[40,41], a decrease in oxidative damage[42], inhibition of several enzymes or transcription factors[43], and an exchange of sulfhydryl groups[44]. In addition, some viewpoints hold that AF could target the tumor microenvironment[45]. Currently, the widely accepted interpretation of AF as an anti-cancer drug is inhibition of the active site to the selenol group[46-48]. Therefore, AF efficiently inhibits the biological function of TrxR, which maintains redox balance and neutralizes reactive oxygen species (ROS), playing a critical role in cell survival and defense mechanism[49,50]. TrxR is a dimeric luteinase that belongs to the pyridine nucleotide disulfide reductase family and is widely expressed at all levels of cells from prokaryotes-to-humans. The TrxR protein family has three isoenzymes (TrxR1, TrxR2, and TrxR3). TrxR1 is widely distributed in the cytoplasm. TrxR1 has a flexible C-terminal containing a cysteine/selenocysteine redox center[51] that endows the interaction of TrxR1 with various substrates and inhibitors. AF, a TrxR1 inhibitor, has an IC_{50} irreversible inhibition of 20 nM[52]. Inhibition of TrxR activity leads to an increase in the ROS concentration and promotes apoptosis of tumor cells[53,54]. The tendency of Au(I) binding to thiols on protein is not particularly surprising because of Au(I) is commonly used to introduce heavy atom positions in X-ray crystallography. AF has also been reported as a precedent for modifying cysteine residues other than catalytic redox[55,56]. Recently, Pickering et al.[57] observed direct binding of an Au atom in AF with a selenium atom in TrxR1 using extended X-ray absorption fine structure (EXAFS) spectroscopy. However, there is still a lack of understanding of the interaction between AF and TrxR1 at the molecular level, especially the absence of microstructure information at the AF-TrxR1 interface and the competitive edge against Trx. As the only known reductant of Trx at present, the extent to which TrxR1 is damaged by AF is an urgent problem in need of clarification.

Nanomaterials have emerged as a potent force in biomedicine. Studies conducted by Shao et al.[58], Jannatun et al.[59], and Song et al.[60] described the roles of nanomaterials in destabilizing cancer cell processes, enhancing immuno-oncotherapy, and converting 'cold' tumors to 'hot' tumors for improved therapy. Luo et al.[61] demonstrated the use of nanomaterials in modulating the tumor microenvironment for enhanced immunotherapy. Zhang et al.[62,63] developed nanomaterials effective against SARS-CoV-2, while Zhang et al.[64] explored the importance of cytokines in nanoimmunosafety. The synergistic potential of these nanomaterials with AF is highlighted for the ability to enhance anti-cancer effects, as noted by Zhang et al.[65] with respect to photothermal nanoagents. Additionally, Wu et al.[66] contributed to the field by producing anti-viral cobalt hydroxide LDH nanosheets, which showcased the versatility of nanomaterials in addressing cancer and viral challenges. These collective works underscored the significant promise of nanomaterials in the future of therapeutic strategies. The potential of AF as a chemosensitizer was investigated to enhance the efficacy of the chemotherapeutic drug, doxorubicin (DOX), in drug-sensitive (B16F10) and -resistant (B16F10/ADR) melanoma cancer cells. The combined treatment with AF not only reduced TrxR activity but also potentiated the pro-oxidant effects of DOX, resulting in a significant accumulation of ROS and subsequent cell death. The interaction of AF with TrxR1 was characterized using molecular docking to identify the binding site, followed by molecular dynamics simulations to confirm complex stability and molecular mechanics-Poisson-Boltzmann surface area (MM-PBSA) calculations to assess binding affinities, which were subsequently validated using surface plasmon resonance (SPR) assays. In summary, our research underscores the potential of AF as a chemosensitizer to overcome multidrug resistance in cancer therapy by resensitizing drug-resistant cells to DOX through redox modulation, offering a theoretical basis for clinical application of AF as an anti-cancer agent.

Materials and methods

Experimental materials

AF was obtained from MedChemExpress (Shanghai, China). DOX and TrxR activity detection kits were purchased from Solarbio Lifesciences Co., Ltd. (Beijing, China). An Apoptosis Detection kit was purchased from Yeason Co., Ltd. (Shanghai, China). An ROS Detection kit was purchased from Beyotime Biotechnology Co., Ltd. (Beijing, China). Dulbecco's modified Eagle medium (DMEM), RPMI-1640 medium, fetal bovine serum (FBS), penicillin-streptomycin, and trypsin were purchased from Hyclone (Logan, Utah, USA).

Cell models

The melanoma cell line, B16F10, was purchased from the American Type Culture Collection (ATCC) (Manassas, VA,

USA) and reanimated from the Laboratory of Inflammation and Vaccine (Shenzhen Institute of Advanced Technology, Shenzhen, China) and cultured with DMEM containing 10% FBS at 37°C in 5% CO_2 and 95% humidity. DOX-resistant melanoma cancer cells (B16F10/ADR) were constructed by inducing B16F10 and MCF-7 with DOX in our laboratory.

Cell cytotoxicity, combination index, and intracellular ROS generation assay *in vitro*

To evaluate the toxicity of different treatments [DOX (8 μM), AF (0.5 μM), or DOX plus AF] toward tumor cells (B16F10 cells). The B16F10 cells were seeded into 24-well plates at a density of 1×10^4 cells/well. The dosage administration was determined based on previous reports[67,68]. After 24 h of culture DOX (8 μM), AF (0.5 μM), or DOX plus AF was added to the medium and cultured for an additional 24 h. Cell viability was assessed using the CCK-8 method. Specifically, after 24 h of culture the medium was aspirated and replaced with medium containing 10% CCK-8 reagent. The cells were then incubated for an additional 3 h and transferred to 96-well plates (100 μL per well). The absorbance value at 450 nm was measured using a microplate reader (each group had 3 replicates).

The cells were exposed to AF (0, 0.5, 1, 2, 4, or 8 μM) or DOX (0, 6.25, 12.5, 25, 50, or 100 μM) for 24 h to confirm the IC_{50} of a single drug in B16/ADR or HepG2 cells. The IC_{50} of combination drugs was detected using the following doses of AF and DOX [1:1, 1:8, or 1:16 (all in μM)]. Cell viability was detected by measuring the OD value at 450 nm using a microplate reader. Fitted data were obtained by non-linear curve fitting based on a logistic model. The combination index (CI) of each combination in B16/ADR or HepG2 cells was calculated using the following formula: $CI = (IC_{50})_{AF}/(IC_{50})'_{AF} + (IC_{50})_{DOX}/(IC_{50})'_{DOX}$. The $(IC_{50})'_x$ represents the concentration of AF or DOX to realize 50% cytotoxicity in combination therapy. $(IC_{50})_x$ represents concentrations of AF or DOX that achieve 50% cytotoxicity in monotherapy. A CI > 1 indicated an antagonistic effect, a CI = 1 indicated an additive effect, and a CI < 1 indicated a synergistic effect.

B16F10 cells were seeded into 6-well plates at a density of 5×10^4 cells/well in a 5% CO_2 environment at 37°C and cultured for 24 h to determine intracellular ROS generation. The cells were subsequently treated with fresh medium containing DOX (8 μM), AF (0.5 μM), or DOX plus AF. After another 24 h of culturing the medium in each well was removed and thrice-washed with PBS. Then, 2′−7′-dichlorodihydrofluorescein diacetate (DCFH-DA) was added to each well [10 μM (200 μL)]. After a 30-min incubation the cell morphologies were observed using fluorescence microscopy and the mean fluorescence intensity was analyzed using flow cytometry (CytoFLEX LX; Beckman, USA).

The toxicity of different treatments [DOX (4 μM), AF (0.5 μM), or DOX plus AF] toward HepG2 cells was determined. The HepG2 cells were seeded into 24-well plates at a density of 1×10^4 cells/well following culture for 24 h. DOX (4 μM), AF (0.5 μM) or DOX plus AF was added to the medium and cultured for an additional 24 h. Cell viability was assessed using the CCK-8 assay. The absorbance value at 450 nm was measured using a microplate reader (each group had 3 replicates).

Intracellular TrxR1 levels in various cell models

To confirm the TrxR1 levels in various cell models under different treatments, cells (B16F10, B16/ADR, or HepG2) were seeded into 6-well plates at a density of 5×10^4 cells/well in a 5% CO_2 environment at 37 °C and cultured for 24 h. Intracellular TrxR in various cell models was detected with a TrxR Activity Detection kit (Solarbio Lifesciences Co., Ltd. Beijing, China) by measuring the OD value at 412 nm using a microplate reader.

In vitro apoptosis analysis

B16F10 and B16F10/ADR cells were cultured in 6-well plates at a density of 1×10^5 cells per well. These cells were subsequently treated with DOX (8 μM), AF (0.5 μM), or DOX plus AF for 24 h. The cells and supernatant were collected and washed at 1,000 g for 3 min. The collected cells were labeled with FITC-Annexin V and propidium iodide (PI) using an Apoptosis Detection kit (Yeason Co., Ltd. Shanghai, China). FITC-Annexin V^+/PI^- cells were identified as early-stage apoptotic cells, while FITC-Annexin V^+/PI^+ cells were considered late-stage apoptotic cells. The data analysis was performed with flow cytometry.

Cancer patient survival data analysis

The association between TrxR1 expression and cancer patient survival was analyzed using publicly available transcriptomic datasets. Renal and liver cancer patient cohorts were retrieved from the Human Protein Atlas (HPA) (https://www.

proteinatlas.org/)[69]. Renal cancer cohort [877 samples with TrxR1 (gene: TXNRD1)] expression was quantified as fragments per kilobase million (FPKM). Patients were stratified into high- [FPKM > 29.7 (n = 208)] and low-expression groups [FPKM < 12.9 (n = 669)] based on distribution quartiles. Liver cancer cohort (365 samples with TrxR1) expression thresholds were set at a FPKM > 69.7 [high (n = 78)] and < 15.6 [low (n = 287)].

Statistical analysis was used for sorting the data. Survival probabilities were compared between the high- and low-expression groups *via* Kaplan-Meier analysis with statistical significance assessed by the log-rank test (renal cancer, $P = 6.3 \times 10^{-7}$; liver cancer, $P = 1.1 \times 10^{-5}$). All data were derived from histologically confirmed cancer tissues and raw expression values are accessible through the HPA portal[70].

Simulation details

The crystal structures of TrxR1 (3EAN), Trx (1ERT), and the Trx/TrxR1 complex (3QFB) were obtained from the Protein Data Bank (PDB). The AF conformation was constructed by Materials Studio and optimized using the Hartree-Fock method with a 6–31 + G* basis set (**Figure 3A**). Therefore, the possible AF binding site on TrxR1 was determined using the flexible docking program, AutoDock (version 4.2.6)[71]. Two-step docking procedures were performed, as follows: (1) "global docking" was used to screen possible binding sites from the entire surface of the protein; and (2) "local docking" was used to find the most likely orientations on the binding site. The search-space size of global docking was 126 Å × 126 Å × 126 Å with a grid spacing of 1.0 Å and the center of the box was set to the geometric center of the protein. In the local docking search the grid box was as small as 60 Å × 60 Å × 60 Å with a grid spacing of 0.375 Å. The center of the box was set as the position of the Se atom in TrxR1 residue Sec498. The Au parameters[72] were added to the AutoDock parameter file. One hundred Lamarckian genetic algorithm (LGA) runs were performed in global and local docking. The root mean square deviation (RMSD) cut-off for cluster analysis was 4.0 Å in global docking and 2.0 Å in local docking.

Docking of Trx to TrxR1 was performed using the ZDOCK Server [http://zdock.umassmed.edu (version 3.0.2)][73]. Global and local docking were sequentially carried out and 10 conformers were produced in each docking. The conformers were ranked by the scoring functions consisting of IFACE statistical potential, shape complementarity, and electrostatics. The stability of the predicted structures was further validated by MD simulations. The structure with the lowest binding energy in the largest cluster was selected as the initial structure for the MD simulations. All simulations were performed with NAMD2.12 package[74] using a 2 fs timestep. The CHARMM27 force field[75] was applied to the protein and the general Amber force field (GAFF)[76] was used for AF. The partial charges of AF were obtained from the restrained electrostatic potential (RESP) calculation[77]. The TIP3P water model[78] was used in this work. The temperature was maintained at 310 K by a Langevin thermostat[79] using a $1ps^{-1}$ damping constant. The pressure was maintained at 1.01 bar using the Langevin piston algorithm[80]. The short-range electrostatic distance and van der Waals energies cut-off was 12 Å. The particle-mesh Ewald (PME) method[81] was used to account for long-range electrostatic interactions. Each system underwent 5,000 steps of energy minimization before production ran. All simulation snapshots were rendered with the VMD program[82].

SPR analysis

The AF/TrxR1 and Trx/TrxR1 system binding affinities were experimentally measured using the Biacore T200 system (GE Healthcare, USA) at 25 °C. The running buffer was PBS-P (consisting of 10 mM phosphate buffer, 137 mM NaCl, 2.7 mM KCl, and 0.05% surfactant P20). First, the target protein (TrxR1) was immobilized onto the surface of the CM5 chip through the amine-coupling method. The immobilization level of TrxR1 reached ~12,000 resonance units (RU). Subsequently, AF or Trx was injected with various concentrations (ranging from 7.81–250 nM for AF and 0.44–14.25 μM for Trx) in the running buffer at a flow rate of 30 μL/min. The contact time was 60 s and the dissociation time was 300 s. Data were analyzed with the Biacore evaluation software [T200 (version 2.0)] by fitting curves with a 1:1 binding model. All SPR experiments were repeated three times independently.

Immunoblotting assay

The B16/ADR cell protein samples with various treatments were used for Western blot analysis. SDS/PAGE gels (12.5%) were prepared for electrophoresis and 35 μg of protein was added to each lane. After blocking with 5% BSA in PBST, the caspase-3 antibody (9662, 1:1000; CST) and cleaved caspase-3 antibody (9661, 1:1000; CST) were selected as the first

antibody. Goat anti-mouse IgG [91196, 1:1000 (HRP conjugate); CST] was used as the secondary antibody.

Results

TrxR1 expression in cancer patient survival analysis

Emerging evidence suggests that TrxR1 overexpression may serve as a prognostic biomarker across multiple cancer types, although the clinical relevance remains incompletely defined. To investigate the translational significance of TrxR1 dysregulation, the association with patient survival using population-scale transcriptomic data was investigated. Whether renal or liver cancer, the survival rates of patients with high levels of TrxR1 protein expression are very low (**Figure 1**), as shown by data from the HPA[69]. This redox adaptation is particularly critical in chemotherapy-resistant tumors, in which amplified antioxidant capacity may counteract pro-oxidant therapies, like DOX.

Chemosensitizing effect of Au on DOX by ROS assays

DOX is a potent anti-cancer agent that has garnered great interest in research due to its high efficacy but the application in cancer therapy has been limited due to drug resistance and poor internalization. Because AF has been used in tumor treatment as a radiation sensitizer[83], we hypothesized that AF could enhance the therapeutic effects of chemo-drugs by disrupting the redox balance as a TrxR inhibitor. The drug-resistant melanoma cancer cell line, B16F10/ADR, was established to conduct corollary studies. To confirm the AF-enhanced chemotherapeutic effects of DOX, three different combinations (AF: DOX = 1:1, 1:8, or 1:16) were used to screen and obtain the optimal combination dose of AF with DOX. The Chou Talalay method was used to analyze the synergistic effects of combined mediation by calculating the CI, including the synergistic effect (CI < 1), additive effect (CI = 1), and antagonistic effect (CI > 1). An IC_{50} of AF and DOX in B16/ADR cells was first detected, as shown by values of 2.87 and 27.89, for calculating CI in various combinations (**Figure S1**). The CI and IC_{50} were both decreased significantly when the AF:DOX ratio was 1:16, as indicated by a CI = 0.51 and IC_{50} = 9.41 μM. Therefore, the combination ratio was determined to be AF:DOX = 1:16. To emphasize the synergistic effect in further research, even when low doses of the two drugs were applied, the DOX and AF dosages were set at relatively low concentrations compared to the individual IC_{50} values, while maintaining the combination ratio at 1:16. Therefore, the concentrations of AF and DOX were set at 0.5 and 8 μM, respectively.

B16F10 and B16F10/ADR cell viability was determined with different treatments. As expected, DOX had limited tumoricidal capacity due to DOX-resistance in B16F10/ADR cells. Notably, the administration of AF plus DOX exhibited

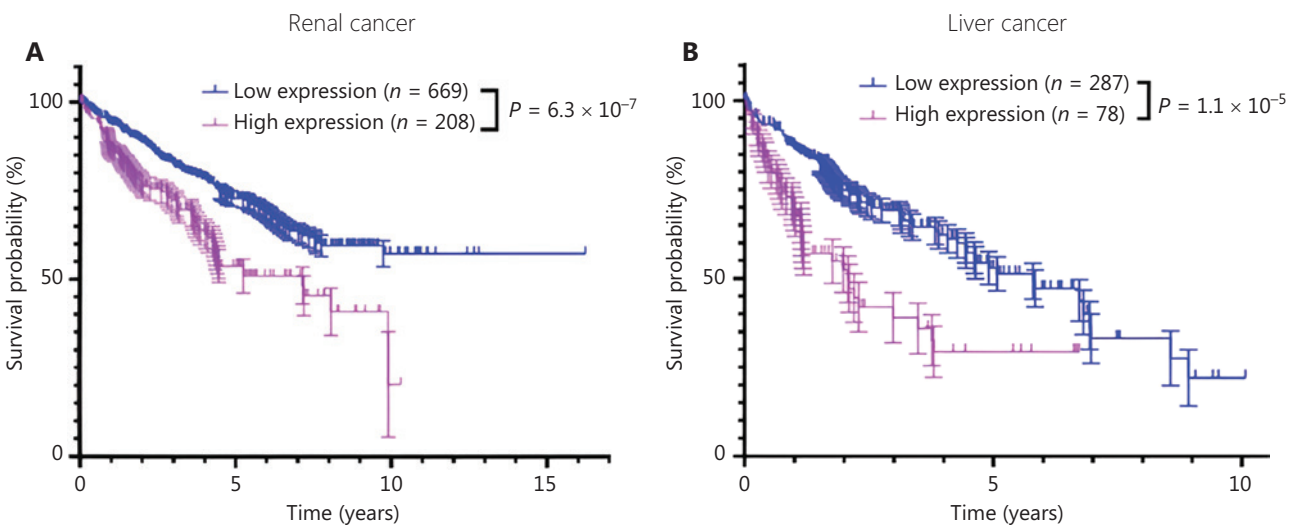


Figure 1 Relationship between TrxR1 expression and survival probability of cancer patients. (A) Among renal cancer patients. (B) In liver cancer patients.

anti-tumor performance in B16F10 and B16F10/ADR cells, indicating the function of AF as a chemotherapy drug sensitizer (**Figure 2A**). It has been reported that TrxR1 is overexpressed in melanoma[84]. In addition, TrxR1 expression was investigated in B16F10 cells and compared to a liver cancer model (HepG2) with high TrxR1 levels[85]. High TrxR1 levels were noted in both cell models with no significant differences (**Figure S2**). In addition, as shown in **Figure 2B**, increased TrxR activity in DOX-treated tumor cells, especially DOX-resistant tumor cells, was observed because due to the antioxidant capacity of tumor cells. When the cells were treated with chemo-drugs, the Trx antioxidant system with TrxR was activated for counteracting the chemotherapy drug-induced ROS. In contrast, the addition of AF reduced TrxR activity compared to single DOX-treated and control groups. These results further confirmed that AF inhibits TrxR activity in tumor and chemotherapy drug-resistant tumor cells. The intracellular ROS concentration was elevated and free DOX induced high ROS generation in B16F10 cells, resulting in increased apoptosis (**Figure 2C-F**). However, the B16F10/ADR cells had relatively low ROS and apoptosis levels when treated with free DOX due to chemoresistance. Interestingly,

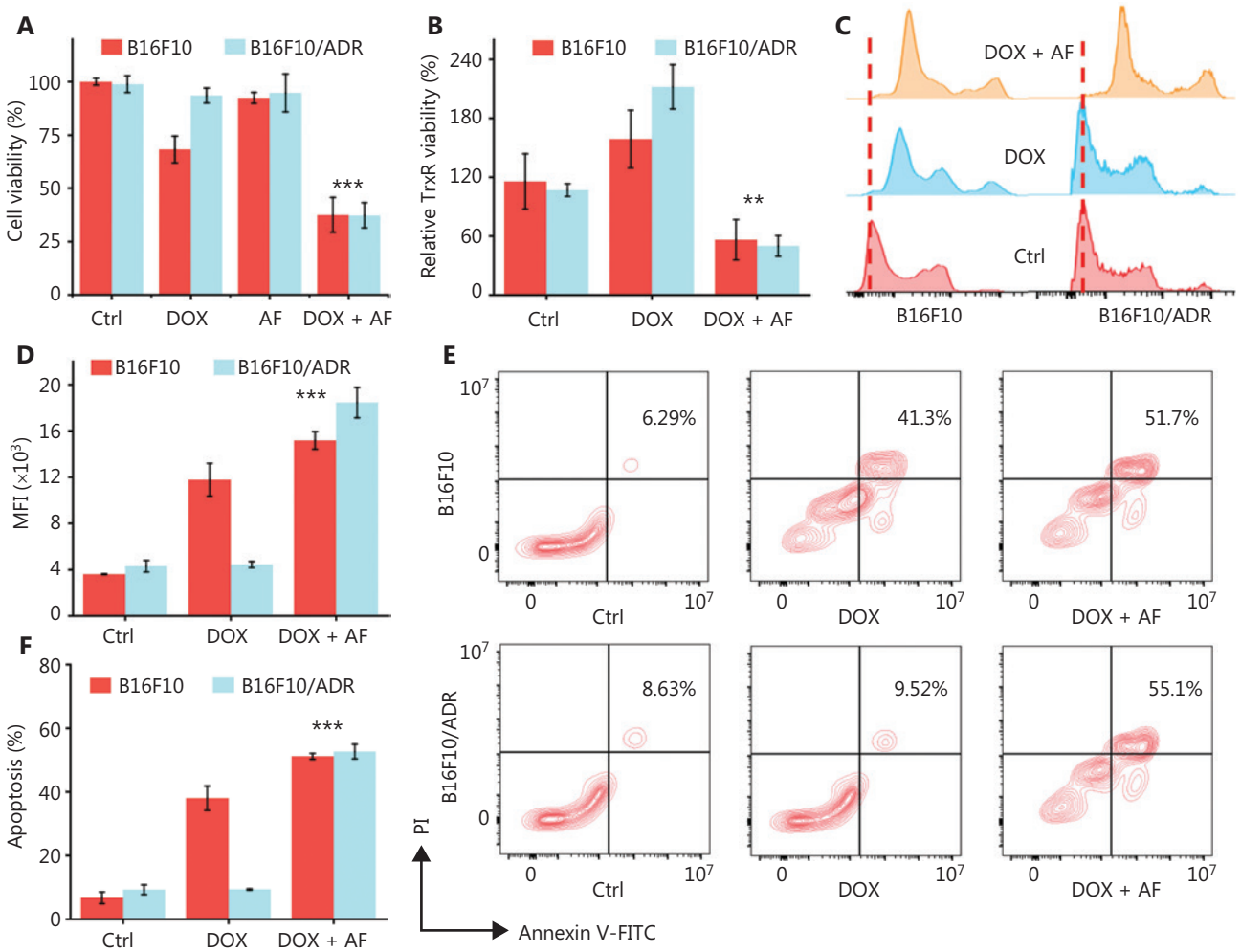


Figure 2 Sensitizing effect of AF with DOX for an anti-ADR effect in the B16F10/ADR cell model *in vitro*. (A) Viability of B16F10 or B16F10/ADR cells exposed to DOX (8 μM), AF (0.5 μM), or DOX plus AF. (B) Intracellular TrxR activity of B16F10 or B16F10/ADR cells exposed to DOX (8 μM), AF (0.5 μM), or DOX plus AF. (C–F) Cytotoxicity of B16F10 or B16F10/ADR cells exposed to DOX (8 μM), AF (0.5 μM), or DOX plus AF. (C) Flow cytometry (FCM) analysis of ROS accumulation. (D) Quantitative analysis of ROS accumulation in panel C. (E) FCM analysis of cell apoptosis. (F) Quantitative analysis apoptosis. Data are presented as the mean ± SD (n = 3). Statistical significance (**P < 0.01; ***P < 0.001) was obtained by two-way ANOVA with LSD multiple comparisons test in A, B, D, and F.

the administration of DOX plus AF demonstrated the best tumor killing ability with evidence of enhanced ROS and cellular apoptosis in all cells compared to the free DOX-treated groups. The results suggested that AF enhances DOX-induced free intracellular ROS, leading to effectively tumor killing in normal and DOX-resistant cells.

The enhanced chemosensitizing effect of DOX combined with AF was also investigated in HepG2 cells, a liver cancer cell model. The IC_{50} of single agent and different combinations was determined for confirming the CI (**Figure S3**). The AF:DOX = 1:8 combination exhibited synergistic effects with CI = 0.93 *vs.* other combinations (AF:DOX = 1:1 or 1:16) had higher CIs (~1.47 and 1.88). Thus, the combination ratio (AF:DOX = 1:8) was used for further research. A similar experimental design was used for anti-tumor assays with B16/ADR cells. The DOX and AF doses were set at relatively low concentrations (0.5 and 4 μM) compared to the individual IC_{50} values, in which the single reagent had limited cytotoxicity toward HepG2 cells. Moreover, the synergistic effect was emphasized when low doses of two drugs were used. Notably, administration of AF plus DOX exhibited anti-tumor performance in HepG2 cells, indicating AF function as a chemotherapy drug sensitizer in various cell models (**Figure S4**).

Global docking of Au to TrxR1

The structure of the Trx/TrxR1 complex determined by X-ray crystallography, which showed that the active site of TrxR1 is

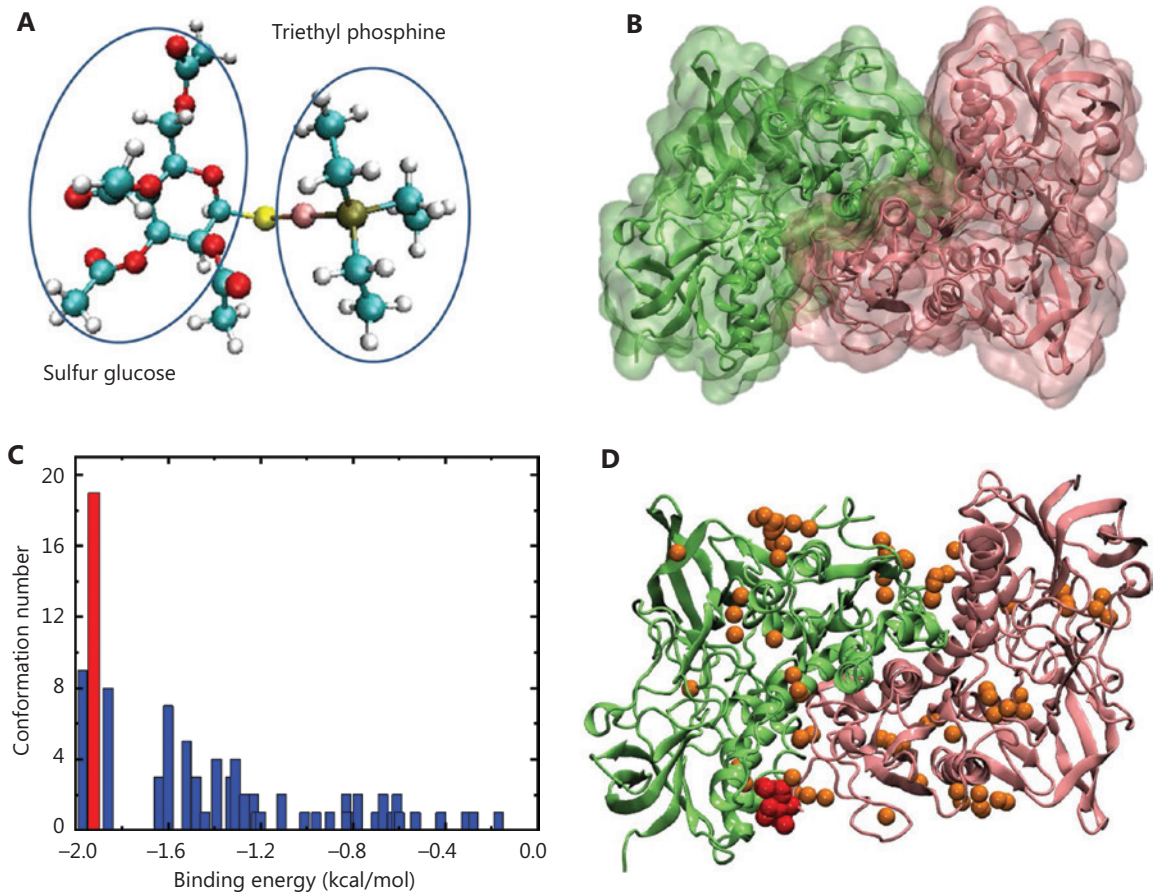


Figure 3 Global docking of AF to TrxR1. (A) Atomic structure of AF, consisting of a triethyl phosphine (2,3,4,6-tetra-O-acetyl-β-1-D-thiopyranosato-S) and sulfur glucose bonded by an Au(I) atom. (B) Conformation of TrxR1 presented by a transparent surface and opaque cartoon. TrxR1 is composed of two homologous chains (chain A in pink and chain B in green). (C) Clustering analysis of the top 100 global docking results. RMSD cut-off for clustering was 4 Å. The cluster with the maximum number of conformers was highlighted in red. There were 19 conformers in this cluster. The position of this cluster was the nearest to the active site of TrxR1. (D) Distribution of the top 100 possible positions of AF on TrxR1. The positions of AF were denoted by the Au atom in AF (orange VDW ball). Red represents the conformers in the biggest cluster.

located at the selenenyl-sulfide motif near the C-terminus[86]. Because of the strong thiol-gold interactions[54], the Au atom in AF prefers to coordinate with the SH/SeH groups in the active site. Therefore, residue Sec498, the active site of TrxR1, is also the AF binding site. Nineteen of 100 conformers targeted the binding site appropriately in the global docking (**Figure 3C**). The minimum distance between Au and Se of the cluster was 3.85 Å. The lowest binding energy (calculated by AutoDock 4.2) was −1.92 kcal/mol, which ranked second.

Local docking of AF to TrxR1

The lowest binding energy of the conformer was up to −4.52 kcal/mol in local docking (**Table S1**). There were 11 conformers in the largest cluster. The conformer with the lowest binding energy (−4.13 kcal/mol) in this cluster was the representative structure (**Figure 4A**). The distance between Au and Se was 2.59 Å in the representative structure, which was the closest distance in all docking results. The AF binding site was in a cave-like structure consisting of the interface between two chains of TrxR1. Importantly, this site was partially overlaid with the Trx binding side. The TrxR1 residues that had direct contact with AF are depicted in **Figure 3B**. Among the TrxR1 residues, residue Ala26, Leu112, and Ile347 in chain B form a hydrophobic interaction with AF and LYS29 form a hydrogen bond with AF by NZ–HZ···O1.

Interaction between AF and TrxR1

The results of 150 ns MD simulations showed that AF is stably bonded with TrxR1. The distance between the Au and Se atoms increased slightly and were stable at approximately 7.45 Å (**Figure 5B**). The RMSD of TrxR1 was approximately 2.26 Å for the last 80 ns (**Figure 5C**). Interestingly, the MRSD of residues that are close to AF (within 4 Å) is almost the same as the TrxR1. Those key residues are the major contributor to

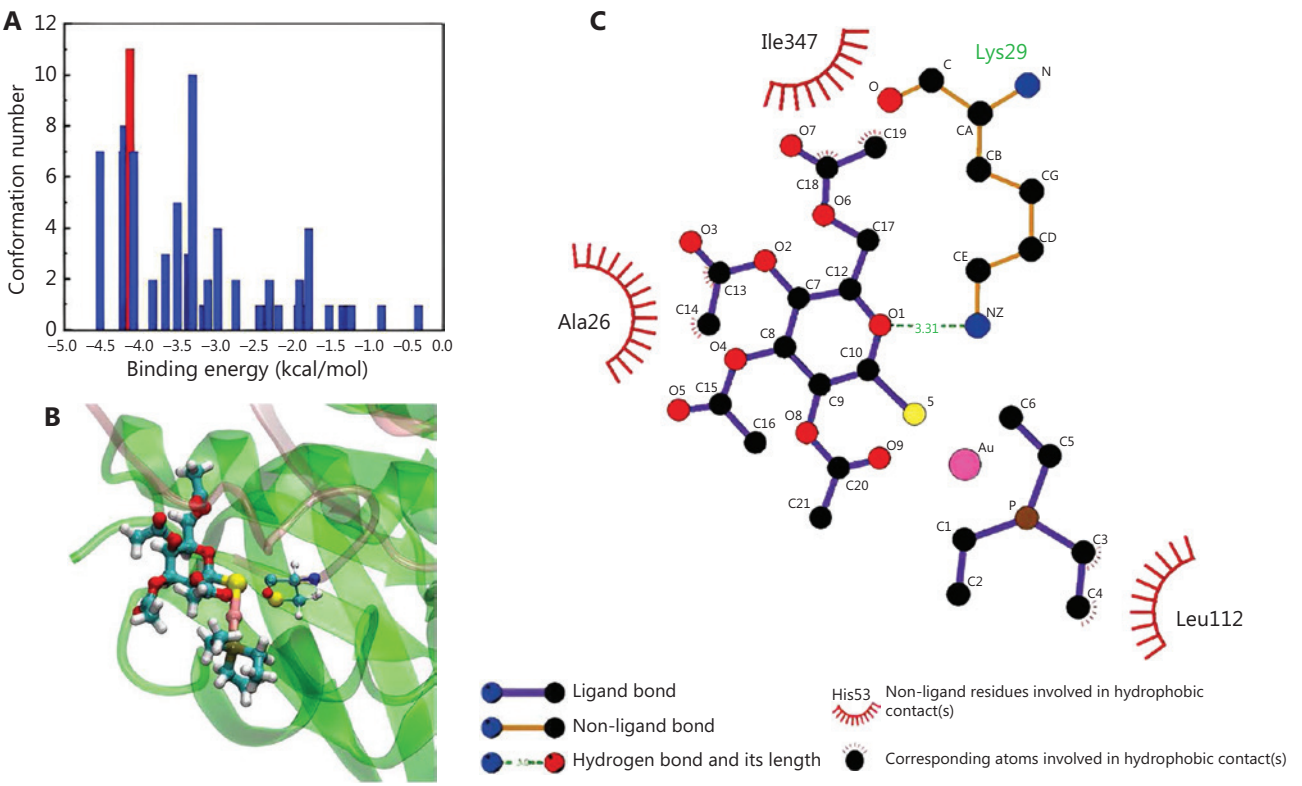


Figure 4 Local docking of AF to TrxR1. (A) The clustering analysis of top 100 conformers. The RMSD cut-off for clustering was 2 Å. The cluster with the maximum number of conformers[11] is denoted by red. (B) The representative structure in the biggest cluster. The binding free energy of this structure was −4.13 kcal/mol. The Au atom in AF is pink, the Se atom in selenocysteine is yellow, and the distance between Au and Se was 2.59 Å. (C) Sketches of AF bounds with TrxR1. The amino acids and hydrogen bonds in direct contact with AF are depicted using the LIGPLOT program[87].

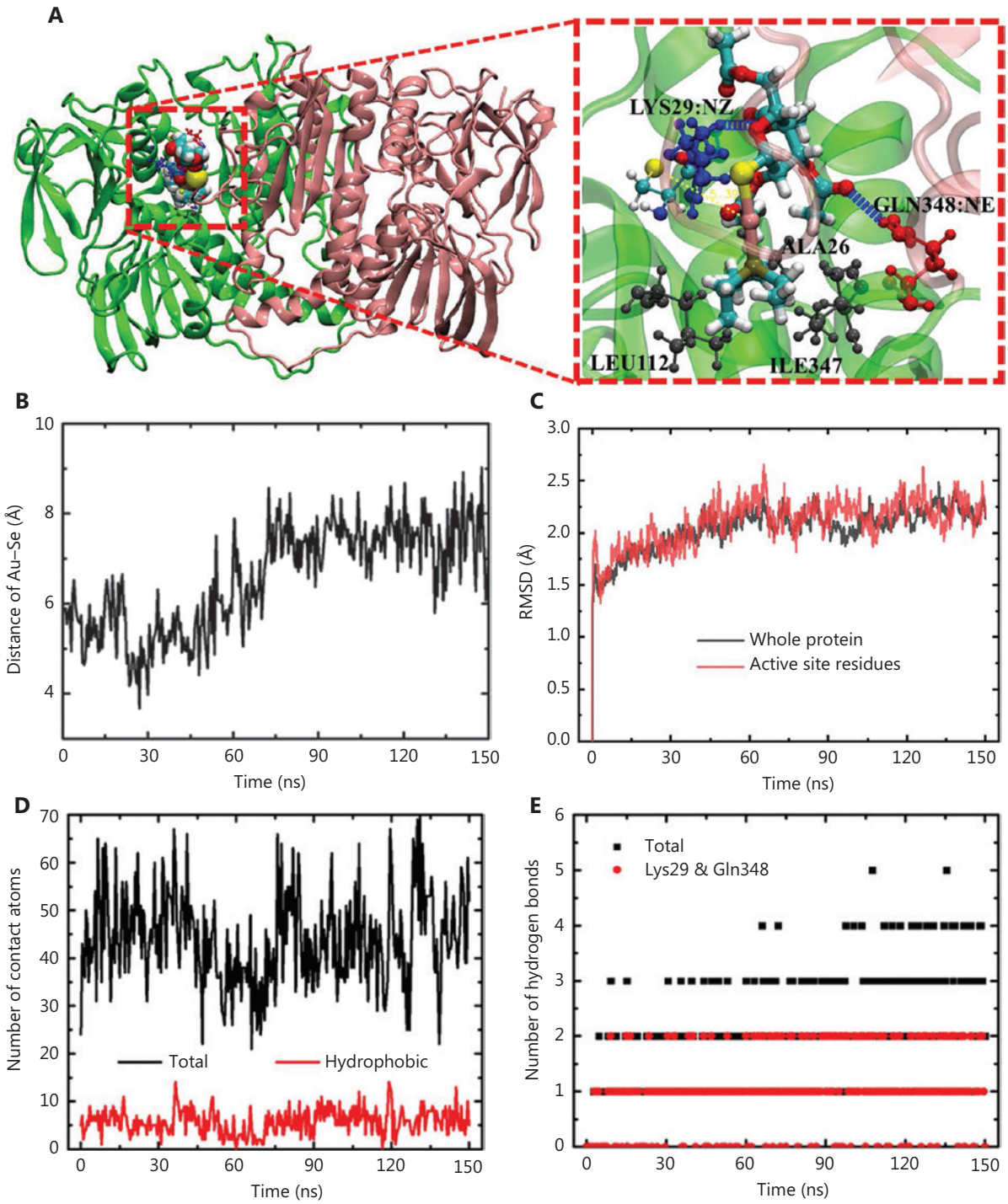


Figure 5 MD simulating the interaction between AF and TrxR1. (A) The conformation of AF@TrxR1 complex at 150 ns. The right panel is the zoom-in of the red square region of the left panel. Chain A is pink and chain B is green. The Ala26, Leu112, and Ile347 residues had hydrophobic interactions with AF are shown in black. Lys29 and Gln348 formed hydrogen bonds with AF are shown in blue and red, respectively. (B) The time-dependent distance between the Au atom of AF and the Se atom of Sec498 in TrxR1. (C) The RMSD of TrxR1 (black line) and RMSD of the residues close to AF (red line) after interacting with AF. (D) The number of contact atoms, total contact (black), and hydrophobic contact (red). (E) The total number of hydrogen bonds formed in the AF@TrxR1 complex (black square); the number of hydrogen bonds formed in AF/Lys29 or AF/Gln348 (red dot).

MRSD. This finding suggests that the effect of AF on TrxR1 is limited to the amino acids near AF.

The AF binding mode with TrxR1 was explored further. The MD results showed that binding of AF to TrxR1 is largely attributed to the hydrophobic interaction, hydrogen bond interaction, and salt bridge (**Figure 5A**). The contact number was defined as the heavy atom pairs that are within 4.0 Å and the hydrophobic contact number was restricted to hydrophobic residues (Ala, Val, Leu, Ile, Phe, Trp, Met, and Pro) on protein with the triethyl phosphine part on AF. The geometry criteria for the hydrogen bond were set to a donor-acceptor distance < 3.5 Å and the donor-hydrogen-acceptor angle < 30°[88]. The total contact number was approximately 50, wherein the hydrophobic contact number was approximately 8 (**Figure 5D**). The residues that had hydrophobic interactions with AF were Ala26, Leu112, and Ile347. AF forms a maximum of five hydrogen bonds with TrxR1. Among them, NZ–HZ···O1 between Lys29 (chain B) and AF/Lys29, and NE2–HE2···O5 between GLN348 (chain B) and AF/GLN348 occur with a high frequency during the 150 ns simulation. The time for co-existence of these two hydrogen bonds accumulated to 118 ns, accounting for 78.7% of the total simulation time (**Figure 5E**).

A mutant simulation (LYS29 and GLN348 on TrxR1 are mutated to GLY) was conducted to better illustrate how the critical residues affect the binding behaviors of AF to TrxR1. The global docking results (**Figure 6**) showed that there were only seven conformers in the largest cluster. The minimum distance between Au and Se of this cluster was 4.88 Å. The binding energy was −1.83 kcal/mol. A further MD simulation was also performed based on this conformation. The distance between Au and Se increased quickly from 4.88 Å to 5.97 Å and gradually increased beyond 9 Å during the 100 ns simulation (**Figure S5**). AF ultimately detached from the mutated TrxR1. This finding indicated that LYS29 and GLN348, which form hydrogen bonds with AF, have a critical role in the binding process.

Inhibition of AF to the formation of TrxR1/Trx complexes

A ternary complex of AF@TrxR1/Trx was constructed to illustrate AF inhibition in formation of TrxR1/Trx complexes. The TrxR1/Trx complex was built using the docking method. The top 10 conformers of the TrxR1/Trx complex predicted by global and local docking were obtained. Six conformers targeted the active site of TrxR1 in global docking (**Table S1**). The conformer with the lowest RMSD compared to the crystal structure (PDB ID 3QFB) was 5.6 Å (rank No. 4). Among all the local docking conformers, the conformer with the lowest RMSD was 5.1 Å (rank No. 1). Residue Trp31 in Trx fit well into the hydrophobic pocket of TrxR1 in this conformation. Trx contacts with residues Gln106, Ile109, Gly110, and Ser111 in chain B of TrxR1 (**Figure 7A** left). Then, the conformations of AF@TrxR1 and TrxR1/Trx complexes were merged to obtain the conformation of the AF@TrxR1/Trx ternary

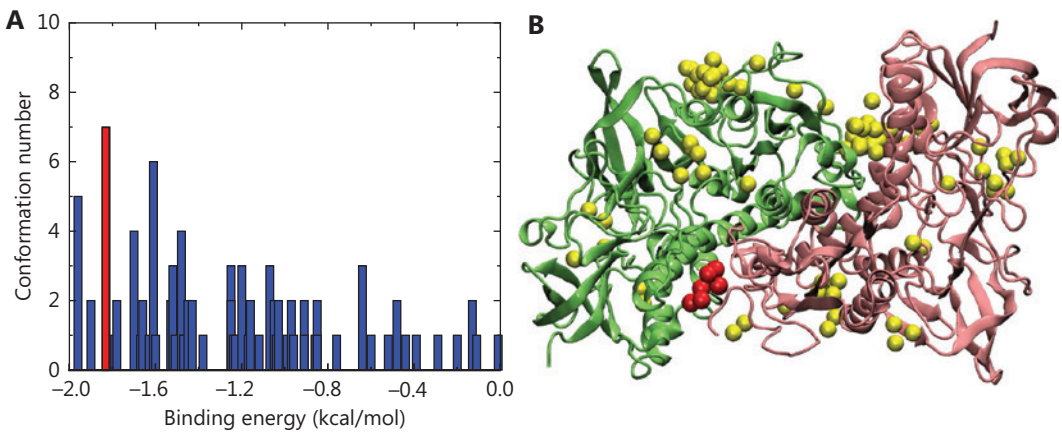


Figure 6 Global docking of AF to mutated TrxR1. (A) Clustering analysis of the top 100 conformers. The RMSD cut-off for clustering was 4 Å. The cluster with the maximum number of conformers is highlighted in red. There were 7 conformers in this cluster. (B) Distribution of the top 100 possible positions of AF on mutated TrxR1. The positions of AF are denoted by the Au atom in AF (yellow VDW ball). Red represents the active site of TrxR1 targeted.

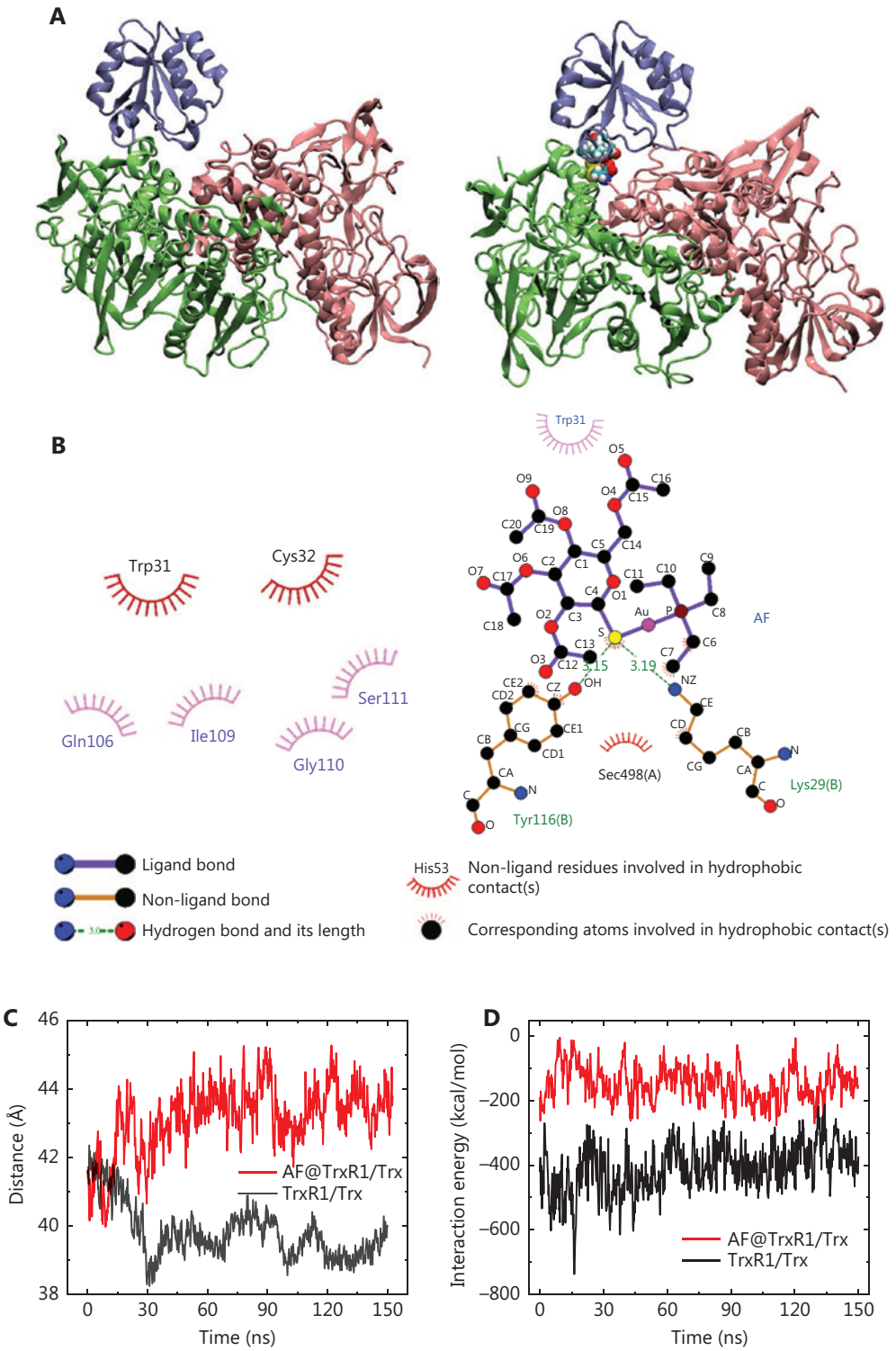


Figure 7 Inhibition of AF to the formation of TrxR1/Trx complex. (A) Conformation of the TrxR1/Trx (left) and AF@TrxR1/Trx complexes (right). The pink and green cartoon modes were the two chains of TrxR1 and the cyan cartoon chain was Trx. AF was shown as a VDW ball. (B) Residues in direct contact with each other in the Trx/TrxR1 (left) and AF@TrxR1/Trx systems (right) were highlighted and visualized by the LIGPLOT+ program. (C) The COM distance between TrxR1 and Trx in the TrxR1/Trx (black line) and AF@TrxR1/Trx systems (red line). (D) The interaction energy between the TrxR1 and Trx in TrxR1/Trx (black line) and AF@TrxR1/Trx systems (red line).

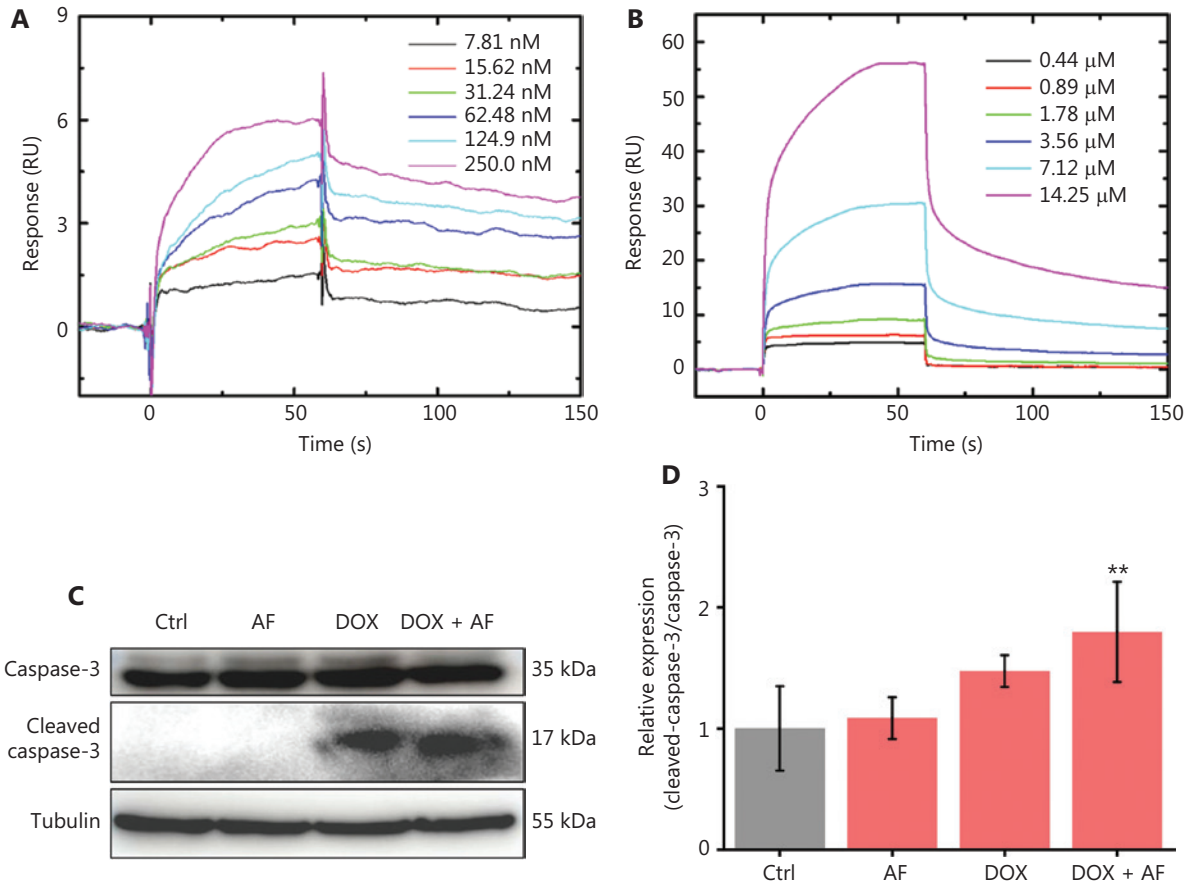


Figure 8 The affinities of AF/TrxR1 and Trx/TrxR1 systems based on the SPR assay. (A) The SPR assay of the AF/TrxR1 system. A series of AF concentrations (7.81 nM–250 nM) were passed over the TrxR1-immobilized sensor chip to obtain the affinity measurement. (B) The SPR assay of the Trx/TrxR1 system. A series of Trx concentrations (0.44 μM–14.25 μM) were passed over the TrxR1-immobilized sensor chip. The SPR experiments were independently repeated three times. (C) Western blot detection of the specific protein expression involved in reducing ADR. Tubulin was used as a loading control. (D) Quantitative analysis of protein expression. The relative protein expression was normalized to the control group. Data are presented as the mean ± SD (n = 3). The statistical significance (**P < 0.01) was obtained by two-way ANOVA with LSD multiple comparisons.

complex (**Figure 7A** right). The binding site of AF partially overlaid the binding interface of Trx but was located deeper inside TrxR1 than Trx.

The following 150 ns MD simulations were performed based on the TrxR1/Trx complex and the AF@TrxR1/Trx ternary complex. During the first 30 ns simulations, the center-of-mass (COM) distance between TrxR1 and Trx decreased from 41.62 Å to 38.27 Å in the TrxR1/Trx system, while the COM distance between TrxR1 and Trx increased from 41.62 Å to 44.26 Å (**Figure 6C**). In the following 120 ns these 2 distances oscillated in the range of 39.21 ± 0.33 Å and 43.68 ± 0.60 Å. The interaction energy between TrxR1 and Trx was also compared. The interaction energy between TrxR1 and Trx in TrxR1/Trx was −355.04 ± 60.84 kJ/mol and −152.22 ± 46.33 kJ/mol in AF@TrxR1/Trx. These results indicated that AF disturbed the interaction between TrxR1 and Trx.

The binding energy of AF/TrxR1 and Trx/TrxR1 systems were estimated using the MM/PBSA method. The binding energy of each atom was compared. Atoms in contact (distance within 4.0 Å) were considered to have contributed to the binding free energy. There were approximately 28 atoms contacting TrxR1 for AF, while the number of contact atoms was approximately 113 for Trx (**Figure S6A**). The binding free energy (ΔG_{bind}) of the AF/TrxR1 interaction was estimated at −187.98 kcal/mol and the per-atom decomposed

energy ranged from −10.5 to −6.4 kcal/mol. Although Trx/TrxR1 system had the lower total binding energy, the per-atom energy was approximately −4.1 kcal/mol, which was higher than the AF/TrxR1 system (**Figure S6B**). Therefore, AF had a stronger binding affinity than Trx in TrxR1 binding.

Binding affinity comparison of AF *vs.* Trx to TrxR1 using the SPR assay

Finally, the SPR assay was used to compare the binding affinity between AF/TrxR1 and Trx/TrxR1 systems. The affinity constant K_D value of the AF/TrxR1 system was 13.24 ± 5.51 nM (n = 3), while the K_D value of the Trx/TrxR1 system was 1.15 ± 0.7 μM (n = 3), as shown in **Figure 8**. The SPR results demonstrated that the affinity of AF to TrxR1 was much stronger than Trx (approximately 87-fold), which was consistent with the theoretical simulation. Zou et al.[89] reported the binding affinity between TrxR1 and the TrxR1 inhibitor, piperlongumine (PL), to be a K_D value of 22.2 μM. By comparison, AF has a stronger binding affinity than PL (K_D decreased by 19-fold). Additionally, a molecular docking experiment showed that PL has the same binding site (residue Cys-498) as AF. An immunoblotting assay was performed to determine the specific protein involved in reducing drug resistance. As shown in **Figure 8C**, caspase-3 signaling was activated by treatment with DOX plus AF with evidence of increased cleaved-caspase-3 expression. In agreement with the cell experiment and theoretical simulation data, the blotting results further showed that the DOX and AF combination led to apoptosis in DOX-resistant B16F10 tumor cells.

Discussion

The potential of AF to amplify the therapeutic effects of chemotherapy drugs was investigated in the current study. The AF and DOX combination was shown to significantly enhance tumor suppression and promote apoptosis in DOX-resistant B16F10/ADR tumor cells using regular (B16F10) and drug-resistant (B16F10/ADR) melanoma cells. This finding was due to the ability of AF to suppress TrxR activity, which was typically elevated in response to chemotherapy as a cellular antioxidant defense. By disrupting this redox balance, AF not only increased intracellular ROS levels but also promoted cellular apoptosis, effectively overcoming chemoresistance. In essence, AF acts as a potent sensitizer, boosting the tumoricidal capabilities of DOX. Furthermore, the mechanism underlying AF inhibition of TrxR1 at the molecular level was also investigated using a combination

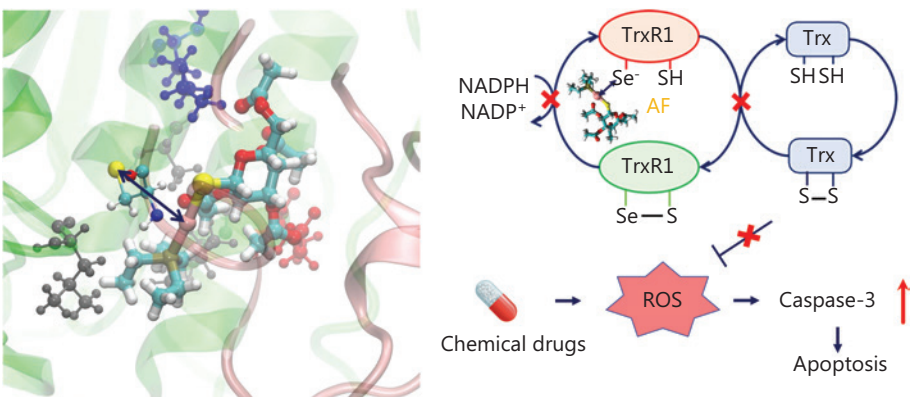


Figure 9 Mechanism underlying AF enhances the cytotoxic effects of DOX in melanoma cells. Auranofin (AF) exerts its effect by targeting the redox-active site of thioredoxin reductase 1 (TrxR1). As illustrated in the left panel, AF is represented as a molecular structure interacting with the catalytic site of TrxR1. TrxR1, shown as a new cartoon with its active site containing a selenocysteine (Sec) residue. The two-way arrow connects the selenium (Se) atom of the Sec residue and the Au atom in the AF molecule. This catalytic site is constituted by Lys29 (blue), Gln348 (red), and Leu112 (black). It has been demonstrated that AF binds with high affinity to the Sec residue within the catalytic site of TrxR1, partially overlapping with the binding site of the endogenous substrate, thioredoxin (Trx), but with greater avidity. This binding impedes the reduction of Trx by TrxR1. The right panel is the mechanistic pathway. Normally, NADPH oxidation to $NADP^+$ supplies electrons *via* FAD to the TrxR1 redox center, reducing the Cys-Sec bond to the -SH/-SeH groups. Reduced TrxR1 then restores Trx to its active form, scavenging doxorubicin-induced reactive oxygen species (ROS). AF blocks this cascade by trapping TrxR1 in its oxidized state, preventing Trx reduction and causing ROS accumulation that triggers apoptosis, synergistically enhancing chemotherapeutic efficacy.

of theoretical simulation and experiments. The binding modes of both AF/TrxR1 and Trx/TrxR1 systems are presented. AF bound to the active site of TrxR1 with high affinity. The hydrophobic interactions, hydrogen bonds, and salt bridge contributed to stabilization of the AF/TrxR1 complex. Additionally, the mutational docking simulation confirmed that the key residues of TrxR1 in the binding site were LYS29 and GLN348. Binding of Trx to TrxR1 was also significantly interfered by the presence of AF. Importantly, the binding free energies of AF/TrxR1 and Trx/TrxR1 systems were compared. The results of the theoretical calculation and experimental approaches indicated that the affinity of AF to TrxR1 was much stronger than Trx, suggesting that AF is an efficient TrxR1 inhibitor. The schematic diagram of the mechanism is shown in **Figure 9**.

Conclusion

Studying the interaction between AF and TrxR1 will help understand the mechanism and role of TrxR1 at the molecular level and understand the metabolism and transport processes of AF, which will together provide a theoretical basis for the design and synthesis of more efficient drug molecules. These findings guide the development and application of gold compounds like AF for cancer therapy and other redox system-related human diseases and provides theoretical support for the clinical application of AF as an anti-tumor drug, revealing a new avenue to overcome chemoresistance.

Grant support

This work was supported by the National Natural Science Foundation of China (Grant Nos. 82261138630, 32171390, and 32201154) and the Natural Science Foundation of Guangdong Province (Grant Nos. 2023B1515020104 and 2024A1515011244).

Conflict of interest statement

No potential conflicts of interest are disclosed.

Author contributions

Conceived and designed the analysis: Yang Li, Xiaofeng Wang.
Collected the data: Xiaofeng Wang, Yingnan Liu, Guofang Zhang.
Contributed data or analysis tools: Wuqiong Zhang, Zhongda Li, Su Li.
Performed the analysis: Jiaxin Chen, Qi Li, Xiaoman Suo, Yanqiao Zeng.
Wrote the paper: Xiaofeng Wang, Yingnan Liu.

Data availability statement

The datasets generated and analyzed during the current study are available from the corresponding author upon reasonable request.

References

1. Drachman RH, Tepperman J. Aurothioglucose obesity in mouse. Yale J Biol Med. 1954; 26: 394-409.
2. Freyberg RH, Block WD, Levey S. Metabolism, toxicity and manner of action of gold compounds used in the treatment of arthritis. I. Human plasma and synovial fluid concentration and urinary excretion of gold during and following treatment with gold sodium thiomalate, gold sodium thiosulfate, and colloidal gold sulfide. J Clin Invest. 1941; 20: 401-12.
3. Giannini EH, Brewer EJ Jr, Person DA. Auranofin in the treatment of juvenile rheumatoid arthritis. J Pediatr. 1983; 102: 138-41.
4. Muranaka M, Miyamoto T, Shida T, Kabe J, Makino S, Okumura H, et al. Gold salt in the treatment of bronchial asthma--a double-blind study. Ann Allergy. 1978; 40: 132-7.
5. Navarro M, Pérez H, Sánchez-Delgado RA. Toward a novel metal-based chemotherapy against tropical diseases. 3. Synthesis and antimalarial activity in vitro and in vivo of the new gold-chloroquine complex (Au(PPh3)(CQ))PF6. J Med Chem. 1997; 40: 1937-9.
6. Berners-Price SJ, Mirabelli CK, Johnson RK, Mattern MR, McCabe FL, Faucette LF, et al. In vivo antitumor activity and in vitro cytotoxic properties of bis(1,2-bis(diphenylphosphino)ethane) gold(I) chloride. Cancer Res. 1986; 46: 5486-93.
7. Tepperman K, Zhang Y, Roy PW, Floyd R, Zhao Z, Dorsey JG, et al. Transport of the dicyanogold(I) anion. Met Based Drug. 1994; 1: 433-43.
8. Lai L, Bi G, Sun Y, Shen M, Su Y, Che X, et al. The formation and release of aurothioglucose from thioglucose-loaded gold nanoparticles by NIR irradiation: a combined anti-cancer effect of thermotherapy and chemotherapy without the risk of uncontrollable drug burst release and leakage. New J Chem. 2021; 45: 22574-8.
9. Xie Z, Wen J, Sun S, Zhang J, Deng X, Han S, et al. In-vitro and in-vivo monitoring of gold(III) ions from intermediate metabolite of sodium aurothiomalate through water-soluble ruthenium (II) complex-based luminescent probe. Bioorg Chem. 2021; 110: 104749.
10. Milani C. Gold concentration in blood after subcutaneous, oral, and rectal introduction as sodium aurothiosulfate. Arch Ital Sci Farmacol. 1957; 7: 129-34.

11. Xu B, Kong W, Li Q, Yang Y, Jiang T, Liu X. A review of thiosulfate leaching of gold: focus on thiosulfate consumption and gold recovery from pregnant solution. Metals. 2017; 7: 222.
12. Chiappetta G, Gamberi T, Faienza F, Limaj X, Rizza S, Messori L, et al. Redox proteome analysis of auranofin exposed ovarian cancer cells (A2780). Redox Biol. 2022; 52: 102294.
13. Jia C, Zhang F, Lin J, Feng L, Wang T, Feng Y, et al. Black phosphorus-Au-thiosugar nanosheets mediated photothermal induced anti-tumor effect enhancement by promoting infiltration of NK cells in hepatocellular carcinoma. J Nanobiotechnol. 2022; 20: 90.
14. Liu Y, Lu Y, Xu Z, Ma X, Chen X, Liu W. Repurposing of the gold drug auranofin and a review of its derivatives as antibacterial therapeutics. Drug Discov Today. 2022; 27: 1961-73.
15. Yu Y, Zhao H, Lin J, Li Z, Tian G, Yang YY, et al. Repurposing non-antibiotic drugs auranofin and pentamidine in combination to combat multidrug-resistant gram-negative bacteria. Int J Antimicrob. 2022; 59: 106582.
16. Blodgett Jr RC. Auranofin: experience to date. Am J Med. 1983; 75: 86-9.
17. Kean WF, Kean IRL. Clinical pharmacology of gold. Inflammopharmacology. 2008; 16: 112-25.
18. Debnath A, Parsonage D, Andrade RM, He C, Cobo ER, Hirata K, et al. A high-throughput drug screen for *Entamoeba histolytica* identifies a new lead and target. Nat Med. 2012; 18: 956-60.
19. Schuh E, Pflüger C, Citta A, Folda A, Rigobello MP, Bindoli A, et al. Gold(I) carbene complexes causing thioredoxin 1 and thioredoxin 2 oxidation as potential anticancer agents. J Med Chem. 2012; 55: 5518-28.
20. Oh BM, Lee S-J, Cho HJ, Park YS, Kim J-T, Yoon SR, et al. Cystatin SN inhibits auranofin-induced cell death by autophagic induction and ROS regulation via glutathione reductase activity in colorectal cancer. Cell Death Dis. 2017; 8: e2682.
21. Hatem E, Azzi S, El Banna N, He T, Heneman-Masurel A, Vernis L, et al. Auranofin/vitamin C: a novel drug combination targeting triple-negative breast cancer. J Natl Cancer Inst. 2018; 111: djy149.
22. Yan X, Zhang X, Wang L, Zhang R, Pu X, Wu S, et al. Inhibition of thioredoxin/thioredoxin reductase induces synthetic lethality in lung cancers with compromised glutathione homeostasis. Cancer Res. 2019; 79: 125-32.
23. Abdalbari FH, Martinez-Jaramillo E, Forgie BN, Tran E, Zorychta E, Goyeneche AA, et al. Auranofin induces lethality driven by reactive oxygen species in high-grade serous ovarian cancer cells. Cancers. 2023; 15: 5136.
24. Ghosh C, Gunda V, Hu JN, Zhang L, Zhang YQ, Shen M, et al. Combination nitazoxanide and auranofin treatment has synergistic anticancer activity in anaplastic thyroid cancer and act by enhanced activation of multiple cell death pathways. Cancer Res. 2023; 83: 5505.
25. Mertens RT, Gukathasan S, Arojojoye AS, Olelewe C, Awuah SG. Next generation gold drugs and probes: chemistry and biomedical applications. Chem Rev. 2023; 123: 6612-67.
26. Seo MJ, Kim IY, Lee DM, Park YJ, Cho MY, Jin HJ, et al. Dual inhibition of thioredoxin reductase and proteasome is required for auranofin-induced paraptosis in breast cancer cells. Cell Death Dis. 2023; 14: 42.
27. Shen SY, Shen J, Luo Z, Wang FD, Min JX. Molecular mechanisms and clinical implications of the gold drug auranofin. Coordin Chem Rev. 2023; 493: 215323.
28. Deben C, Boullosa LF, Fortes FR, de la Hoz EC, Le Compte M, Seghers S, et al. Auranofin repurposing for lung and pancreatic cancer: low CA12 expression as a marker of sensitivity in patient-derived organoids, with potentiated efficacy by AKT inhibition. J Exp Clin Cancer Res. 2024; 43: 88.
29. Zhang M, Yang DY, He ZY, Wu Y, Tian XY, Huang QY, et al. Auranofin inhibits the occurrence of colorectal cancer by promoting mTOR-dependent autophagy and inhibiting epithelial-mesenchymal transformation. Anti-Cancer Drugs. 2024; 35: 129-39.
30. Falchetti M, Delgobo M, Zancanaro H, Almeida K, das Neves RN, Dos Santos B, et al. Omics-based identification of an NRF2-related auranofin resistance signature in cancer: insights into drug repurposing. Comput Biol Med. 2023; 152: 106347.
31. Luo JJ, Li Y, Li YR, Chen XF, Du PY, Wang Z, et al. Reversing ferroptosis resistance in breast cancer via tailored lipid and iron presentation. ACS Nano. 2023; 17: 25257-68.
32. Emran TB, Shahriar A, Mahmud AR, Rahman T, Abir MH, Siddiquee MFR, et al. Multidrug resistance in cancer: understanding molecular mechanisms, immunoprevention and therapeutic approaches. Front Oncol. 2022; 12: 891652.
33. Lu YL, Ma XY, Chang XY, Liang ZL, Lv L, Shan M, et al. Recent development of gold(I) and gold(III) complexes as therapeutic agents for cancer diseases. Chem Soc Rev. 2022; 51: 5518-56.
34. Passirani C, Vessières A, La Regina G, Link W, Silvestri R. Modulating undruggable targets to overcome cancer therapy resistance. Drug Resist Update. 2022; 60: 100788.
35. Liu YN, Zhang GF, Li Q, Chen JX, Luo WH, Li XJ, et al. Nano-assemblies overcome cancer multidrug resistance for effectively synergistic chemo-immuno-oncotherapy. Chem Eng J. 2024; 290: 151437.
36. Gamberi T, Chiappetta G, Fiaschi T, Modesti A, Sorbi F, Magherini F. Upgrade of an old drug: auranofin in innovative cancer therapies to overcome drug resistance and to increase drug effectiveness. Med Res Rev. 2022; 42: 1111-46.
37. Jin P, Jiang JW, Zhou L, Huang Z, Nice EC, Huang CH, et al. Mitochondrial adaptation in cancer drug resistance: prevalence, mechanisms, and management. J Hematol Oncol. 2022; 15: 97.
38. Bukowski K, Kciuk M, Kontek R. Mechanisms of multidrug resistance in cancer chemotherapy. Int J Mol Sci. 2020; 21: 3233.
39. Deepika N, Rajendra Prasad N, Radhiga T. Auranofin sensitizes breast cancer cells to paclitaxel mediated cell death via regulating FOXO3/Nrf2/Keap1 signaling pathway. Cell Biochem Funct. 2024; 42: e3903.
40. Godwin AK, Meister A, O'Dwyer PJ, Huang CS, Hamilton TC, Anderson ME. High resistance to cisplatin in human ovarian cancer cell lines is associated with marked increase of glutathione synthesis. Proc Natl Acad Sci U S A. 1992; 89: 3070-4.

41. Gencheva R, Cheng Q, Arnér ESJ. Thioredoxin reductase selenoproteins from different organisms as potential drug targets for treatment of human diseases. Free Radic Biol Med. 2022; 190: 320-38.
42. Daniel LW, Civoli F, Rogers MA, Smitherman PK, Raju PA, Roederer M. ET-18-OCH3 inhibits nuclear factor kappa B activation by 12-O-tetradecanoylphorbol-13-acetate but not by tumor necrosis factor-alpha or interleukin 1 alpha. Cancer Res. 1995; 55: 4844-9.
43. Handel ML, Watts CK, deFazio A, Day RO, Sutherland RL. Inhibition of AP-1 binding and transcription by gold and selenium involving conserved cysteine residues in Jun and Fos. Proc Natl Acad Sci U S A. 1995; 92: 4497-501.
44. Snyder RM, Mirabelli CK, Crooke ST. Cellular association, intracellular distribution, and effux of auranofin via sequential ligand exchange reactions. Biochem Pharmacol. 1986; 35: 923-32.
45. Fiskus W, Saba N, Shen M, Ghias M, Liu J, Gupta SD, et al. Auranofin induces lethal oxidative and endoplasmic reticulum stress and exerts potent preclinical activity against chronic lymphocytic leukemia. Cancer Res. 2014; 74: 2520-32.
46. Marzano C, Gandin V, Folda A, Scutari G, Bindoli A, Rigobello MP. Inhibition of thioredoxin reductase by auranofin induces apoptosis in cisplatin-resistant human ovarian cancer cells. Free Radic Biol Med. 2007; 42: 872-81.
47. Gabbiani C, Mastrobuoni G, Sorrentino F, Dani B, Rigobello MP, Bindoli A, et al. Thioredoxin reductase, an emerging target for anticancer metallodrugs. Enzyme inhibition by cytotoxic gold(III) compounds studied with combined mass spectrometry and biochemical assays. Med Chem Commun. 2011; 2: 50-4.
48. James LRA, Xu Z-Q, Sluyter R, Hawksworth EL, Kelso C, Lai B, et al. An investigation into the interactions of gold nanoparticles and anti-arthritic drugs with macrophages, and their reactivity towards thioredoxin reductase. J Inorg Biochem. 2015; 142: 28-38.
49. Gandin V, Fernandes AP, Rigobello MP, Dani B, Sorrentino F, Tisato F, et al. Cancer cell death induced by phosphine gold(I) compounds targeting thioredoxin reductase. Biochem Pharmacol. 2010; 79: 90-101.
50. Zou P, Chen M, Ji J, Chen W, Chen X, Ying S, et al. Auranofin induces apoptosis by ROS-mediated ER stress and mitochondrial dysfunction and displayed synergistic lethality with piperlongumine in gastric cancer. Oncotarget. 2015; 6: 36505-21.
51. Arnér ESJ, Holmgren A. Physiological functions of thioredoxin and thioredoxin reductase. Eur J Biochem. 2000; 267: 6102-9.
52. Gromer S, Arscott LD, Williams CH Jr, Schirmer RH, Becker K. Human placenta thioredoxin reductase. Isolation of the selenoenzyme, steady state kinetics, and inhibition by therapeutic gold compounds. J Biol Chem. 1998; 273: 20096-101.
53. Soderberg A, Sahaf B, Rosen A. Thioredoxin reductase, a redox-active selenoprotein, is secreted by normal and neoplastic cells: presence in human plasma. Cancer Res. 2000; 60: 2281-9.
54. Fang JG, Lu J, Holmgren A. Thioredoxin reductase is irreversibly modified by curcumin: a novel molecular mechanism for its anticancer activity. J Biol Chem. 2005; 280: 25284-90.
55. Ilari A, Baiocco P, Messori L, Fiorillo A, Boffi A, Gramiccia M, et al. A gold-containing drug against parasitic polyamine metabolism: the X-ray structure of trypanothione reductase from *Leishmania infantum* in complex with auranofin reveals a dual mechanism of enzyme inhibition. Amino Acids. 2012; 42: 803-11.
56. Parsonage D, Sheng F, Hirata K, Debnath A, McKerrow JH, Reed SL, et al. X-ray structures of thioredoxin and thioredoxin reductase from *Entamoeba histolytica* and prevailing hypothesis of the mechanism of Auranofin action. J Struct Biol. 2016; 194: 180-90.
57. Pickering IJ, Cheng Q, Rengifo EM, Nehzati S, Dolgova NV, Kroll T, et al. Direct observation of methylmercury and auranofin binding to selenocysteine in thioredoxin reductase. Inorg Chem. 2020; 59: 2711-8.
58. Shao XM, Ding ZH, Zhou WH, Li YY, Li ZB, Cui HD, et al. Intrinsic bioactivity of black phosphorus nanomaterials on mitotic centrosome destabilization through suppression of PLK1 kinase. Nat Nanotechnol. 2021; 16: 1150-60.
59. Jannatun N, Zhang YQ, Wu B, Song QL, Cao GL, Luo WH, et al. Tea polyphenol coordinated with nanoparticles of zif-8 and coated with polydopamine and peg for immuno-oncotherapy. ACS Appl Nano Mater. 2023; 6: 4379-89.
60. Song QL, Zhang GF, Wang B, Cao GL, Li DJ, Wang Y, et al. Reinforcing the combinational immuno-oncotherapy of switching "cold" tumor to "hot" by responsive penetrating nanogels. ACS Appl Mater. 2021; 13: 36824-38.
61. Luo WH, Zeng YQ, Song QL, Wang Y, Yuan F, Li Q, et al. Strengthening the combinational immunotherapy from modulating the tumor inflammatory environment via hypoxia-responsive nanogels. Adv Healthc Mater. 2024; 13: e2302865.
62. Zhang GF, Cong YL, Liu FL, Sun JF, Zhang JT, Cao GL, et al. A nanomaterial targeting the spike protein captures SARS-CoV-2 variants and promotes viral elimination. Nat Nanotechnol. 2022; 17: 993-1003.
63. Zhang GF, Wang XF, Wang GC, Suo XM, Qiu Y, Luo RH, et al. Nanoparticles insert a three dimensional cavity structure of proteins for function inhibition: the case of CeO2 and SARS-CoV-2. Nano Today. 2024; 55: 102183.
64. Zhang GF, Luo WH, Yang WJ, Li S, Li DJ, Zeng YQ, et al. The importance of the IL-1 family of cytokines in nanoimmunosafety and nanotoxicology. Wiley Interdiscip Rev Nanomed Nanobiotechnol. 2022; 14: e1850.
65. Zhang YQ, Zhang GF, Wang GC, Wu LD, Monteiro-Riviere NA, Li Y. The synergistic strategies for the immuno-oncotherapy with photothermal nanoagents. Wiley Interdiscip Rev Nanomed Nanobiotechnol. 2021; 13: e1717.
66. Wu B, Zhang GF, Ji JW, Luo RH, Chen JK, Liu FL, et al. ZIF-67-Derived antivirus cobalt hydroxide LDH nanosheets produced through high-concentration cobalt ion-assisted hydration. Adv Funct Mater. 2023; 34: 2312941.
67. Scarbrough PM, Mapuskar KA, Mattson DM, Gius D, Watson WH, Spitz DR. Simultaneous inhibition of glutathione- and thioredoxin-dependent metabolism is necessary to potentiate 17AAG-induced

cancer cell killing via oxidative stress. Free Radical Biol Med. 2012; 52: 436-43.
68. Pilco-Ferreto N, Calaf GM. Influence of doxorubicin on apoptosis and oxidative stress in breast cancer cell lines. Int J Oncol. 2016; 47: 753-62.
69. Uhlén M, Fagerberg L, Hallström BM, Lindskog C, Oksvold P, Mardinoglu A, et al. Tissue-based map of the human proteome. Science. 2015; 347: 1260419.
70. Pontén F, Gry M, Fagerberg L, Lundberg E, Asplund A, Berglund L, et al. A global view of protein expression in human cells, tissues, and organs. Mol Syst Biol. 2009; 5: 337.
71. Morris GM, Huey R, Lindstrom W, Sanner MF, Belew RK, Goodsell DS, et al. AutoDock4 and AutoDockTools4: automated docking with selective receptor flexibility. J Comput Chem. 2009; 30: 2785-91.
72. Zsila F, Bikadi Z, Hazai E, Simon A, Fitos I, Mady G. Organogold complexes probe a large beta-barrel cavity for human serum alpha1-acid glycoprotein. Biochim Biophys Acta. 2008; 1784: 1106-14.
73. Pierce BG, Wiehe K, Hwang H, Kim BH, Vreven T, Weng Z. ZDOCK server: interactive docking prediction of protein-protein complexes and symmetric multimers. Bioinformatics. 2014; 30: 1771-3.
74. Phillips JC, Braun R, Wang W, Gumbart J, Tajkhorshid E, Villa E, et al. Scalable molecular dynamics with NAMD. J Comput Chem. 2005; 26: 1781-802.
75. Best RB, Zhu X, Shim J, Lopes PEM, Mittal J, Feig M, et al. Optimization of the additive CHARMM all-atom protein force field targeting improved sampling of the backbone ϕ, ψ and side-chain χ^1 and χ^2 dihedral angles. J Chem Theory Comput. 2012; 8: 3257-73.
76. Wang J, Wolf RM, Caldwell JW, Kollman PA, Case DA. Development and testing of a general Amber force field. J Comput Chem. 2004; 25: 1157-74.
77. Bayly CI, Cieplak P, Cornell WD, Kollman PA. A well-behaved electrostatic potential based method using charge restraints for deriving atomic charges: the RESP model. J Phys Chem. 1993; 97: 10269-80.
78. Jorgensen WL, Chandrasekhar J, Madura JD, Impey RW, Klein ML. Comparison of simple potential functions for simulating liquid water. J Chem Phys. 1983; 79: 926-9.
79. Brünger A, Brooks CL III, Karplus M. Stochastic boundary conditions for molecular dynamics simulations of ST2 water. Chem Phys Lett. 1984; 105: 495-500.
80. Vanommeslaeghe K, Hatcher E, Acharya C, Kundu S, Zhong S, Shim J, et al. CHARMM general force field: a force field for drug-like molecules compatible with the CHARMM all-atom additive biological force fields. J Comput Chem. 2010; 31: 671-90.
81. Darden T, York D, Pedersen L. Particle mesh Ewald: an $N\log(N)$ method for Ewald sums in large systems. J Chem Phys. 1993; 98: 10089-92.
82. Humphrey W, Dalke A, Schulten K. VMD: visual molecular dynamics. J Mol Graph. 1996; 14: 33-38.
83. Wang H, Bouzakoura S, De Mey S, Jiang H, Law K, Dufait I, et al. Auranofin radiosensitizes tumor cells through targeting thioredoxin reductase and resulting overproduction of reactive oxygen species. Oncotarget. 2017; 8: 35728-42.
84. Bjørklund G, Zou L, Wang J, Chasapis CT, Penan M. Thioredoxin reductase as a pharmacological target. Pharmacol Res. 2021; 174: 105854.
85. Dong G, Ye X, Wang S, Li W, Cai R, Du L, et al. Au-24 as a potential thioredoxin reductase inhibitor in hepatocellular carcinoma cells. Pharmacol Res. 2022; 177: 106113.
86. Fritz-Wolf K, Kehr S, Stumpf M, Rahlfs S, Becker K. Crystal structure of the human thioredoxin reductase-thioredoxin complex. Nat Commun. 2011; 2: 383.
87. Laskowski RA, Swindells MB. LigPlot+: multiple ligand-protein interaction diagrams for drug discovery. J Chem Inf Model. 2011; 51: 2778-86.
88. Baker EN, Hubbard RE. Hydrogen bonding in globular proteins. Prog Biophys Mol Biol. 1984; 44: 97-179.
89. Zou P, Xia Y, Ji J, Chen W, Zhang J, Chen X, et al. Piperlongumine as a direct TrxR1 inhibitor with suppressive activity against gastric cancer. Cancer Lett. 2016; 375: 114-26.

Cite this article as: Wang X, Liu Y, Zhang W, Li Z, Li S, Chen J, et al. Beyond gold: the chemoenhancing mechanism and therapeutic potential of auranofin in melanoma. Cancer Biol Med. 2025; 22: 672-689. doi: 10.20892/j.issn.2095-3941.2025.0026